01 Jan 2023

# Additive Manufacturing Of SiC-Sialon Refractory With Excellent Properties By Direct Ink Writing

Ruoyu Chen

Saisai Li

Xinxin Jin

Haiming Wen
*Missouri University of Science and Technology*, wenha@mst.edu



## Recommended Citation

R. Chen et al., "Additive Manufacturing Of SiC-Sialon Refractory With Excellent Properties By Direct Ink Writing," *Journal of the European Ceramic Society*, Elsevier, Jan 2023.
The definitive version is available at https://doi.org/10.1016/j.jeurceramsoc.2023.07.055

Journal of the European Ceramic Society 43 (2023) 7196–7204

Contents lists available at ScienceDirect

Journal of the European Ceramic Society

journal homepage: www.elsevier.com/locate/jeurceramsoc

# Additive manufacturing of SiC-Sialon refractory with excellent properties by direct ink writing

Ruoyu Chen [a,b], Saisai Li [c,*], Xinxin Jin [d], Haiming Wen [b,*]

[a] School of Metallurgical Engineering, Anhui University of Technology, Maanshan, Anhui 243002, China
[b] Department of Materials Science and Engineering, Missouri University of Science and Technology, Rolla, Missouri 65409, USA
[c] School of Materials Science and Engineering, Anhui University of Technology, Maanshan, Anhui 243002, China
[d] China Aerospace Science and Technology Corporation, Beijing 100048, China

ARTICLE INFO

*Keywords:*
3D printing
SiC-Sialon refractory
Rheology
Printing parameters
Complex-shape

ABSTRACT

Additive manufacturing of SiC-Sialon refractory with complex geometries was achieved using direct ink writing processes, followed by pressureless sintering under nitrogen. The effects of particle size of SiC powders, solid content of slurries and additives on the rheology, thixotropy and viscoelasticity of ceramic slurries were investigated. The optimal slurry with a high solid content was composed of 81 wt% SiC (3.5 μm+0.65 μm), $Al_2O_3$ and $SiO_2$ powders, 0.2 wt% dispersant, and 2.8 wt% binder. Furthermore, the accuracy of the structure of specimens was improved via adjustment of the printing parameters, including nozzle size, extrusion pressure, and layer height. The density and flexural strength of the printed SiC-Sialon refractory sintered at 1600 °C were 2.43 g/cm$^3$ and 85 MPa, respectively. In addition, the printed SiC-Sialon crucible demonstrated excellent corrosion resistance to iron slag. Compared to the printed crucible bottom, the crucible side wall was minimally affected by molten slag.

## 1. Introduction

Refractories are materials that resist to decomposition by heat, pressure, or chemical attack, and retain strength and form at high temperatures [1]. SiC-Sialon(SiAlON) is a refractory that has been used in furnaces, reactors and incinerators owing to its high mechanical strength, good high-temperature stability and excellent corrosion resistance. Currently, methods for manufacturing SiC-Sialon refractory include grouting, semi-dry pressing, plastic forming, vibration forming, and hot pressing [2]. However, it is difficult to manufacture SiC-Sialon refractory with complex geometries and high density using these methods.

Additive manufacturing, i.e., 3D priting, is considered an ideal technique for applications demanding complex geometries. Various additive manufacturing techniques have been developed, such as direct ink writing [3], digital light processing [4], binder jetting [5], and selective laser sintering [6]. Direct ink writing is the most popular technique for manufacturing refractories with complex geometries [7]. Zhu et al. manufactured $SiO_2$-$Al_2O_3$ refractory products via direct ink writing and investigated the influence of printing parameters on the structure of the products [7]. Yu et al. successfully fabricated $Al_2O_3$-$SiO_2$ refractory with complex geometries by using a layered extrusion forming method with the optimized slurries [8]. For additive manufacturing techniques, rheology of slurries and printing parameters strongly affect the structure of the final products. However, most researchers have focused on the optimization of viscosity and viscoelasticity of slurries rather than thixotropy [7,8]. Actually, the thixotropy of slurries, which represents the ability of the slurry to rebuild its structure [9], also plays a key role in affecting the stability of the printed preform structure. Currently, the relationships between the rheological and thixotropic behavior of slurries or printing parameters and the structure of printed refractories have not been investigated in details. In addition, the density of refractories greatly influences their mechanical properties and corrosion resistance [10]. High solid content slurries with excellent printability are crucial for manufacturing high-density ceramics/refractories via direct ink writing [11]. However, very limited studies have focused on optimizing the flowability and thixotropy of high solid content slurries to produce dense refractories.

To address these knowledge gaps, this work optimized the rheology and thixotropy of the high solid content slurries by adjusting the particle size distribution of SiC powder, zeta potential, and amounts of dispersant and binder. The influences of printing parameters combined with

* Corresponding authors.
*E-mail addresses:* lisaisai@ahut.edu.cn (S. Li), wenha@mst.edu (H. Wen).

https://doi.org/10.1016/j.jeurceramsoc.2023.07.055
Received 31 May 2023; Received in revised form 20 July 2023; Accepted 21 July 2023
Available online 22 July 2023

**Table 1**
Compositions of the ceramic powder mixtures (wt%).

| | A | B | C | D | E | F |
|---|---|---|---|---|---|---|
| SiC(D50 =3.5 μm) | 80 | / | / | 57.87 | 59.54 | / |
| SiC(D50 =0.65 μm) | / | 80 | / | 22.13 | / | 49.08 |
| SiC(D50 =0.45 μm) | / | / | 80 | / | 20.46 | 30.92 |
| Reactive $Al_2O_3$ | 14 | 14 | 14 | 14 | 14 | 14 |
| Microsilica | 6 | 6 | 6 | 6 | 6 | 6 |

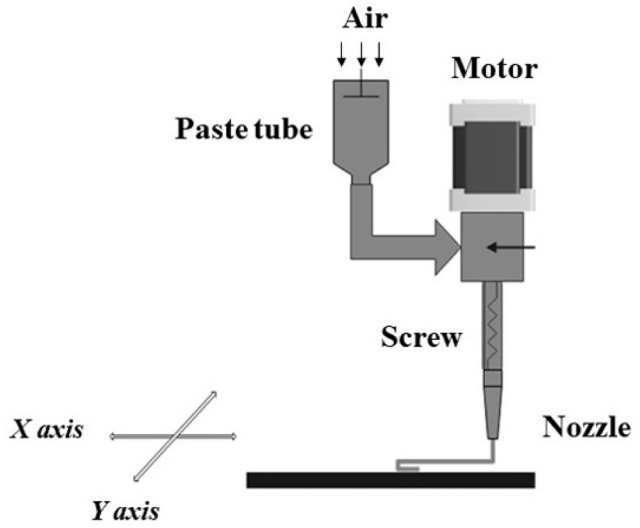


**Fig. 1.** Schematic of the printing system.

the rheology and thixotropy of slurries on the structure of printed preforms were investigated using a fluid field model. Finally, the properties, phase compositions, and microstructure of the printed SiC-Sialon refractory were studied.

## 2. Materials and methods

### 2.1. Slurry preparation

SiC powders (D50 =3.5 μm, D50 =0.65 μm and D50 =0.45 μm, purity ≥ 99 wt%, Weifang Huarong Ceramic Co., Ltd., China), $Al_2O_3$ powder (D50 =2 μm, purity ≥ 98 wt%, Qingdao Almatis Premium Alumina Co., Ltd., China) and silica fume (D50 =1.0 μm, purity ≥96 wt %, Wuxi Chenguan Refractories Co., Ltd., China) were utilized as raw materials. Polycarboxylate (FS20) and sodium alginate were used as dispersant and binder, respectively. Compositions of the powder mixtures for the slurries are shown in Table 1. The particle size distributions of SiC powders in the mixtures D, E and F were calculated using Furnu's theory [12].

Slurries with different solid contents (78 wt%~81 wt%) were prepared by ball milling for 3 h. The milling speed and the ratio of ball to powders were 300 rpm and 2:1, respectively.

### 2.2. Direct ink writing and sintering processes

The printing models were created in Microsoft 3D Builder and exported to G-Code. The code modified by Python was executed by Simplify 3D. The ceramic slurries were printed using a commercial 3D printer (ZCC2000) with a compressed air module to form refractory green bodies through layer-by-layer processes. The structure of the printing system is schematically shown in Fig. 1. After printing, the green bodies were dried at 100 °C for 24 h, and then sintered in nitrogen at 1450–1600 °C for 3 h using pressureless sintering.

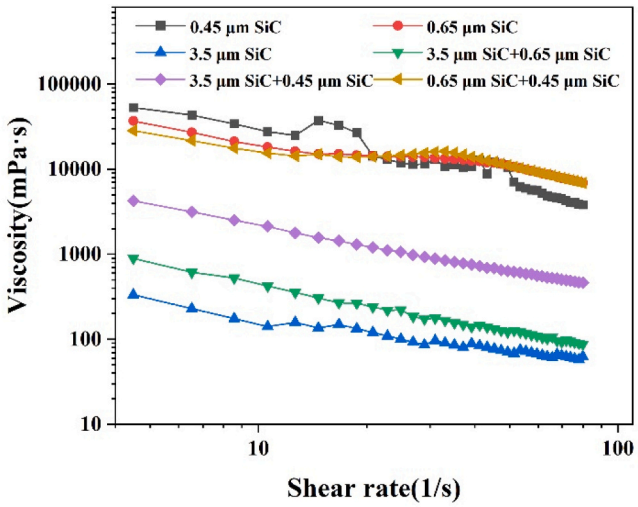


**Fig. 2.** Effect of particle size distribution of SiC powders on the viscosity of the slurries.

### 2.3. Characterization and testing

The rheological properties of the slurries were characterized using a rheometer (Anton Paar MCR 102). Thixotropy index is a ratio of a slurry's viscosity at two different shear rates, generally different by a factor of ten. This value is indicative of a slurry's ability to rebuild its structure [9]. Therefore, in this work, the thixotropy of slurries was evaluated by using the thixotropy index γ (Eq. 1) [13]:

$$\gamma = \frac{\tau_1}{\tau_2} \quad (1)$$

where $\tau_1$ is viscosity at a low shear rate; in this work 5.012 $s^{-1}$ was used. $\tau_2$ represents an increased shear rate, with 50.12 $s^{-1}$ being used for this work. The density and porosity of the manufactured SiC-Sialon refractory were determined using Archimedes method. Three-point bend testing was carried out to measure the flexural strength of the SiC-Sialon refractory samples using an electrical universal testing machine (Instron 5881) with a loading rate of 0.5 mm/s. The testing direction was perpendicular to the manufacturing direction. Thus, stress was applied in direction of the boundaries between the individual layers. The dimensions of the bars for the flexural strength testing were 10 × 10 × 40 mm. Furthermore, the number of layers of the bars was 20. High-temperature~1100 °C exposure followed by water quenching was carried out to evaluate the thermal shock resistance of the SiC-Sialon refractory samples (bars with dimensions of 10 × 10 × 40 mm). After thermal shock cycles, the residual flexural strength of the SiC-Sialon refractory samples was tested (three-point bend testing) at ambient temperature. The residual strength ratio was calculated to evaluate the change in flexural strength before and after water quenching. The phase compositions of the SiC-Sialon refractory samples sintered at different temperatures (1450 °C, 1500 °C, 1550 °C, and 1600 °C) were characterized using X-ray diffraction (XRD, Phillips X'Pert MRD) at ambient temperature. Fracture surfaces of the samples after the flexural tests were analyzed using scanning electron microscopy (SEM, FEI Quanta 200).

## 3. Results and discussion

### 3.1. Rheology of slurries

The preparation of slurries with excellent rheology is essential for the additive manufacturing of SiC-Sialon refractory. The particle size distribution of powder mixtures is crucial in determining the fluidity of the

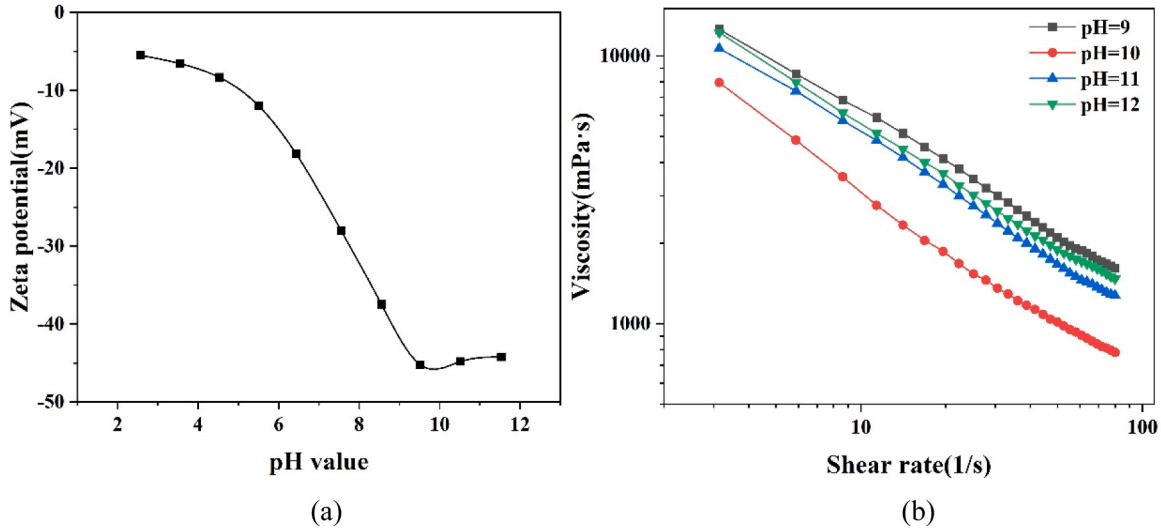


**Fig. 3.** Effects of pH value on the zeta potential and viscosity of the slurries (a) zeta potential and (b) viscosity.

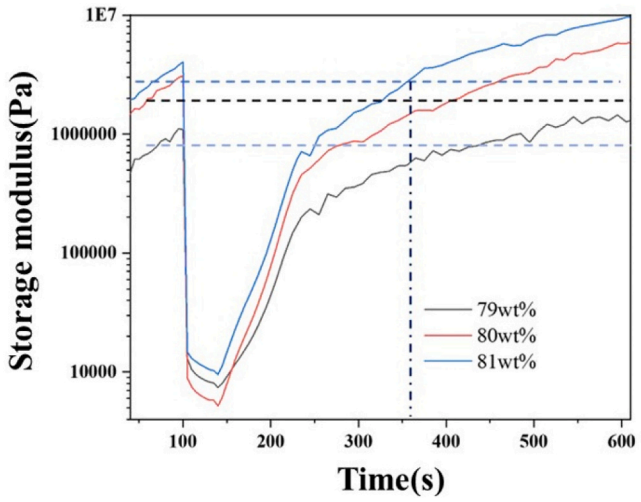


**Fig. 4.** Effect of solids content on the storage modulus of the slurries.

slurries [14]. Fig. 2 illustrates the effect of particle size distribution of SiC powders on the viscosity of the slurries. As the particle size increased, the viscosity of the slurries decreased gradually. The slurries prepared with a bimodal particle size distribution of SiC powders exhibited lower viscosity and superior fluidity in comparison to those prepared with a single particle size, because the particle size distribution influenced the packing density of the packing particles. Adjusting the particle size distribution of the SiC powders helped to reduce the porosity in the powder mixtures, resulting in a denser packing and significantly decreased porosity in the slurries, which, in turn, improved fluidity. In addition, larger SiC powder particles possessed poor sintering ability, and therefore fine SiC powder particles were necessary to improve sintering and overall specimen quality.

Based on the above results, the optimum particle size distribution for mixed powders was found to be 3.5 μm SiC + 0.65 μm SiC. With that, the effects of pH value on the zeta potential and viscosity of slurries were studied. The pH value of the slurry was adjusted using a sodium hydroxide solution. Fig. 3(a) depicts the zeta potential of the slurries at different pH values. As pH value increased, the zeta potential decreased. At around pH~10, the zeta potential reached its maximum, and it increased gradually with a further increase in pH value. Meanwhile, the viscosity of the slurries was strongly impacted by the pH value (Fig. 3 (b)). The minimum viscosity of the slurries was found at pH~10. The uniform distribution of SiC, $Al_2O_3$ and microsilica powders in the slurries was attributed to the surface charge effect of the powders [15]. Therefore, as the pH value was 10, the high solid content slurries with excellent flowability was obtained, which was beneficial to additively manufacturing high-density SiC-Sialon refractory. The results indicated that the optimal pH value for the slurries was 10.

**Table 2**
The thixotropy index of the slurries with different solids contents.

| Solids Content (wt%) | 79 | 80 | 81 |
|---|---|---|---|
| Thixotropy index | 2.32 | 3.27 | 3.89 |

Fig. 4 illustrates the storage modulus of the slurries with varying solids content. As the solids content increased, the storage modulus of the slurries gradually increased, indicating that the slurry structure became more stable with a higher solids content. The reduction in the distance between the powder particles in the slurries enhanced the Van der Waals' forces between the particles, which hindered the flow of the slurries [16]. The solids content of the slurries should not be lower than 78 wt% as this would negatively affect the density, strength, and corrosion resistance of the SiC-Sialon refractory. Despite this, the extruded slurries should maintain good flowability during printing to generate minimal flaws in the green bodies, and thus the solids content should not be too high. Furthermore, increasing the solids content improved the thixotropy of the slurry (Table 2). When the solids content increased, the distance between the powder particles in the slurries decreased, favoring stronger interactions and viscous forces between the particles in the slurries [17]. As a result, slurries with excellent thixotropy stabilized quickly after printing, resulting in very few flaws, such as warpage and collapse, in the green bodies. Based on these findings, slurries with 81 wt% solids content were selected to print the specimens. The Herschel-Bulkley model was used to evaluate the pseudoplastic properties of the inks (Eq. 2) [18]:

$$\tau = \tau_0 + \kappa\gamma^n \tag{2}$$

where $\tau$ is shear stress, $\tau_0$ is yield stress, $\gamma$ is applied shear rate, $\kappa$ is the consistency index, and $n$ is the shear-thinning index. All the slurries showed shear-thinning behavior with shear-thinning indices lower than 1, indicating that they were non-Newtonian fluids. With an increase in solids content, the shear thinning behavior of the slurries was further enhanced, which enabled the slurries to extrude smoothly and rapidly thicken after extrusion.

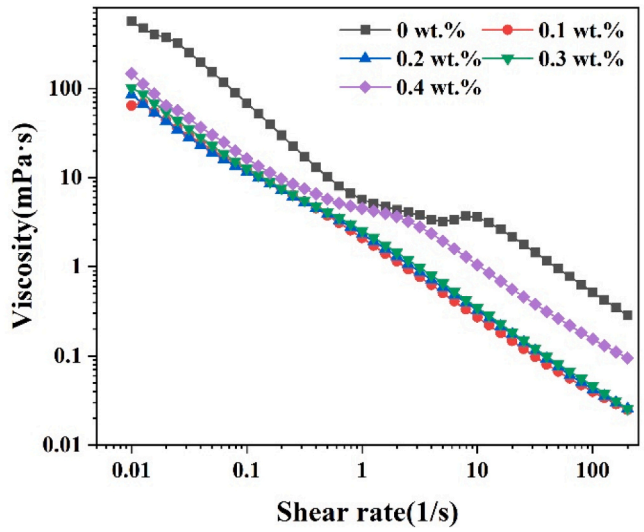


**Fig. 5.** Effect of content of dispersant (FS20) on the viscosity of the slurries.

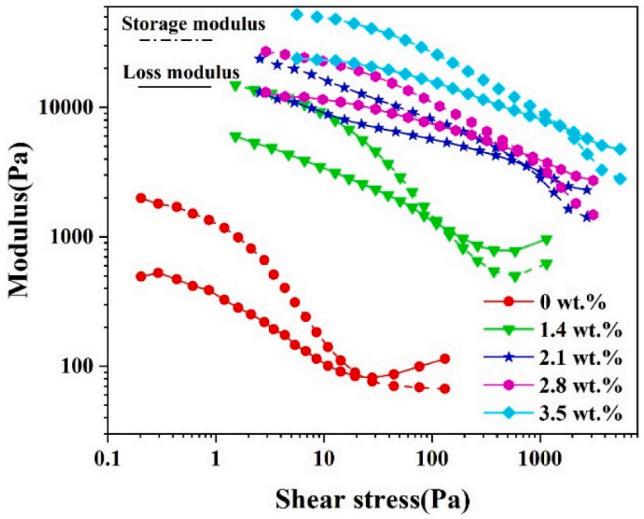


**Fig. 6.** Effect of content of binder (sodium alginate) on the viscoelastic moduli of the slurries.

For direct ink writing, the slurry with good flowability is a reliable guarantee for printing [19]. Polycarboxylate (FS20) was an ideal dispersant for improving the distribution of powder particles in the slurries [20]. Fig. 5 shows the effect of the content of dispersant (FS20) on the viscosity of the slurries. As the content of dispersant increased, the viscosity of the slurries initially decreased and then increased. The minimum viscosity value was achieved at 0.1 wt% dispersant due to the steric hindrance and electrostatic stabilization effects of the dispersant [21]. Nevertheless, adding an excessive amount of dispersant to the slurries generated a network structure caused by the excess and free dispersant molecules, which caused slurry flocculation based on the DLVO theory [22,23]. Therefore, the optimum content of the dispersant was 0.1 wt%.

Afterward, the effects of binder (sodium alginate) addition on the thixotropy and viscoelasticity of the slurries were studied. At low shear stresses, the storage modulus of the slurries was greater than the loss modulus, indicating that the viscous properties of the slurries were dominant (Fig. 6). The shear stress at which the two modulus curves cross over is known as the flow point. Below the flow point, viscous behavior dominates, while above the flow point the behavior of the suspension is predominantly plastic. Among the slurries, the one containing 3.5 wt% sodium alginate exhibited the highest flow point due to the increased stability of the network in the slurries [24]. For 3D printing, thixotropic behavior is critical as it determines the rebuilding speed of slurry structures, which in turn, influences the slurries' ability to retain its shape after extrusion. The thixotropy index of the slurries also increased with the content of sodium alginate (Table 3). The slurries exhibited the best thixotropy when the content of sodium alginate reached 2.8 wt%, owing to the higher rate of the disentanglement of sodium alginate macromolecules by shearing than re-entanglement [23]. However, with further increase in sodium alginate content, the thixotropy of the slurries decreased because of the bridging flocculation caused by excess sodium alginate.

**Table 3**
The thixotropy index of the slurries with different contents of binder (sodium alginate).

| Sodium alginate (wt%) | 0 | 1.4 | 2.1 | 2.8 | 3.5 |
|---|---|---|---|---|---|
| Thixotropy index | 3.89 | 4.58 | 4.79 | 5.10 | 4.53 |

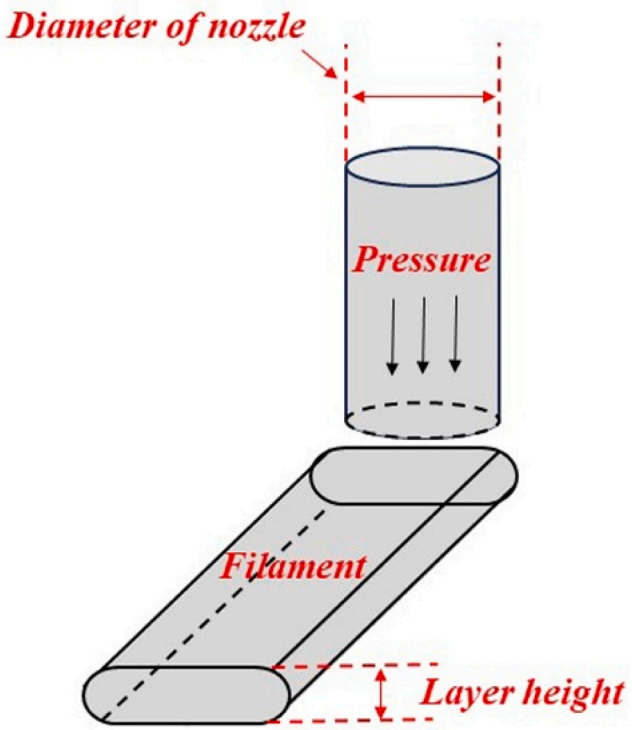


**Fig. 7.** The structure of the printed filament and printing parameters.

### 3.2. The printing parameters

Printing parameters, such as bed temperature, angle for printing, nozzle size, air pressure, and layer height, play a crucial role in determining the structure and dimensional accuracy of printed green bodies [7,25]. When the slurries with excellent rheology and thixotropy were used for printing, the width and height of filament were primarily determined by the nozzle size, air pressure, and layer height (Fig. 7). However, the effects of the above mentioned printing parameters on the shape of SiC-Sialon refractory had not been thoroughly investigated. In this study, optical images of green body structures, combined with shear rate distribution models of slurries, were used to study the effects of printing parameters on the extrusion process and body structures. The morphology of green bodies printed using different nozzle sizes is presented in Fig. 8. As the nozzle size increased, the width of the filament

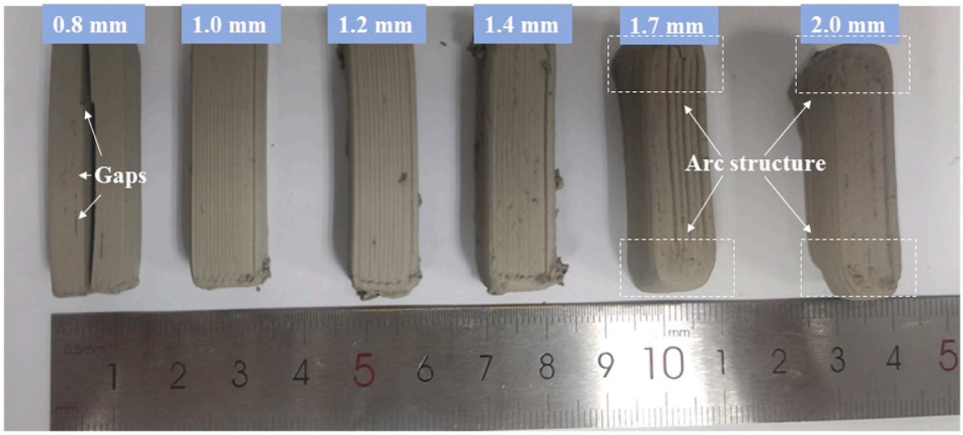


**Fig. 8.** The effect of nozzle size on the structure of green bodies.

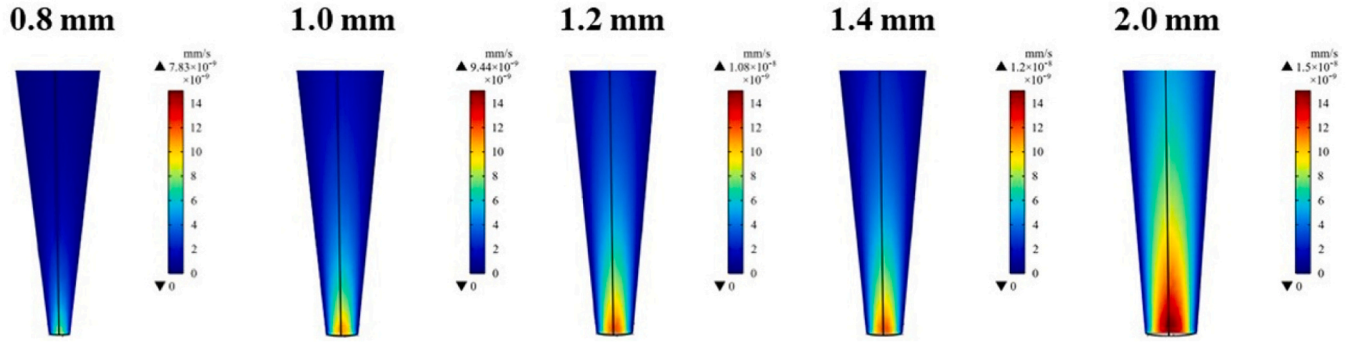


**Fig. 9.** Simulation results depicting the flow rate distribution within the different nozzles.

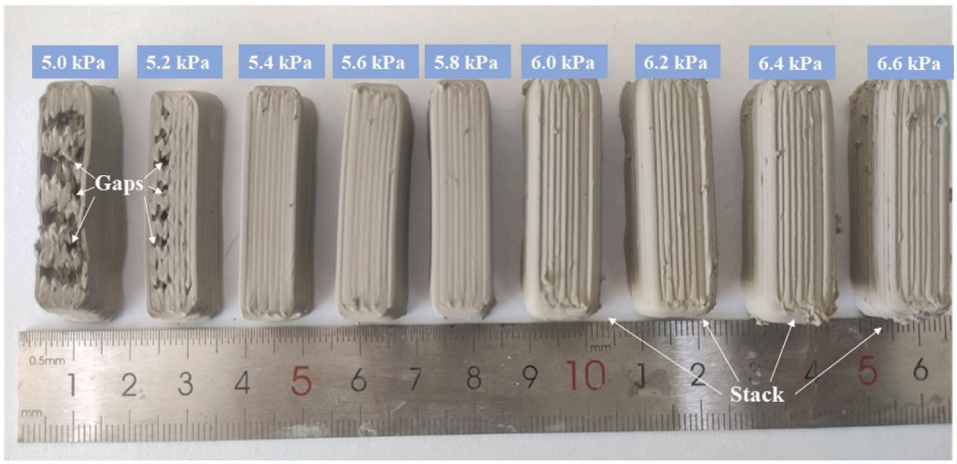


**Fig. 10.** The effect of pressure on the structure of green bodies.

increased, while the dimensional accuracy decreased. Additionally, the edges of the printed filaments built up on the top of each other, resulting in a structure that differed from the model. Consequently, the structure of printed SiC-Sialon refractory, particularly for small parts, was significantly affected. Furthermore, as the diameter of the nozzle increased, the flow speed of the slurries gradually increased (Fig. 9), reducing the viscosity of the slurries due to their shear thinning behavior. The recovery time of the slurry structure also increased, resulting in further differences between the green bodies and the model. However, when the diameter of the nozzle was 0.8 mm, gaps formed between the filaments, which negatively affected the properties of the SiC-Sialon refractory. Therefore, an optimum diameter of the nozzle was selected to be 1.0 mm.

Fig. 10 displays the green bodies printed under varying pressure parameters. As the pressure increased from 5.0 kPa to 6.6 kPa, the width and height of the filaments noticeably increased, while the number of gaps present in the green bodies declined gradually. According to the shear rate distribution model of slurries, employing low air pressure during printing slowed down the slurries' passage through the nozzle (Fig. 11). Consequently, the viscosity of the slurries increased and their

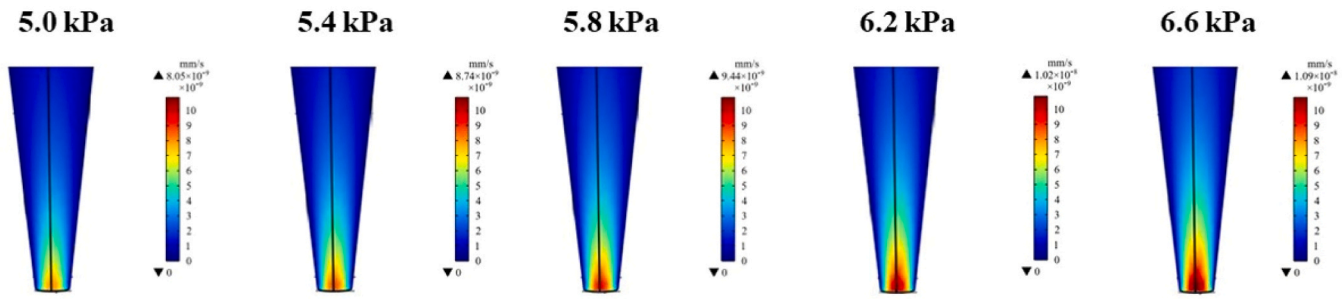


**Fig. 11.** Comsol model of ink flow rate with different applied air pressures.

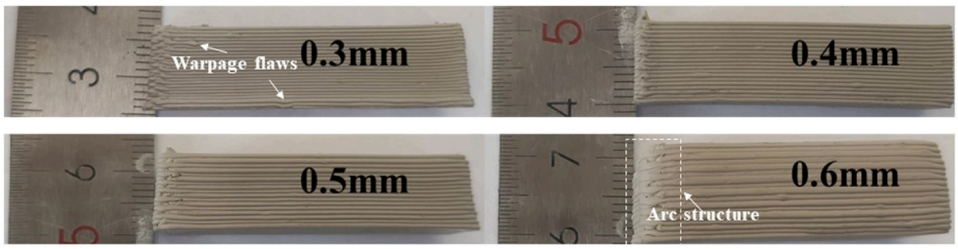


**Fig. 12.** The effect of layer height on the structure of green bodies.

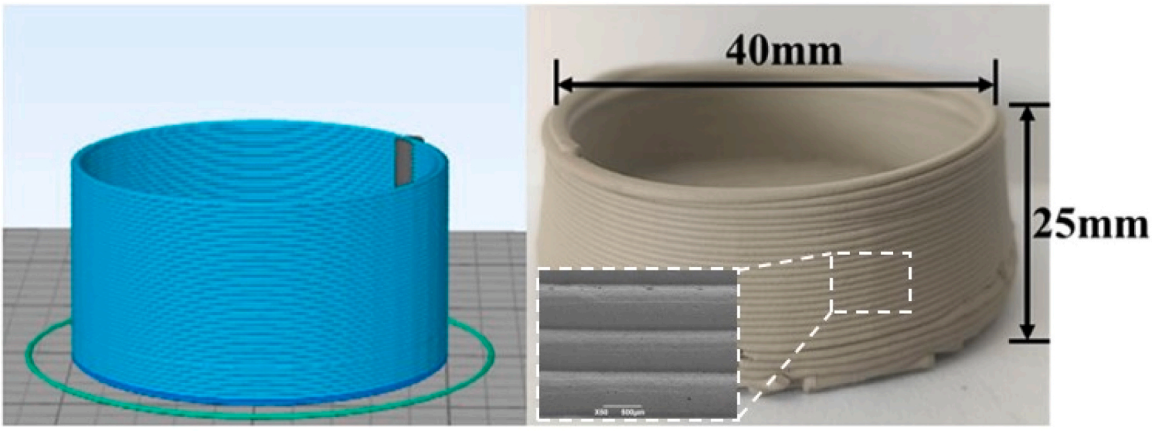


**Fig. 13.** A schematic of model and optical image of SiC-Sialon refractory crucible.

extrusion speed was slower than nozzle speed, leading to the formation of gaps between the filaments. With increasing pressure, the extrusion speed of slurries increased, eventually synchronizing with the nozzle speed and thereby optimizing the structure of the green body. However, a further increase in pressure led to excess slurry piling up on either side of the nozzle, because the low viscosity of the slurries resulted in an extended time required to rebuild the structure of the slurries after leaving the nozzle. Consequently, the optimum pressure for printing was determined to be 5.8 kPa.

According to previous reports, in comparison with other printing parameters, the layer height was found to have the highest correlation with the structure of the filament [19]. The influence of layer height on the structure of green bodies is presented in Fig. 12. It was observed that a layer height of 0.3 mm caused filament warpage and slurry accumulation on the sides of the green body during printing, because the layer height was smaller than the diameter of nozzle. As the layer height increased, the height of the filament also increased gradually, and the number of flaws in the green body decreased. The green bodies printed using a layer height of 0.5 mm were free of deformations. However, further increase in the layer height led to distinct changes in the structure of the green bodies, particularly on the sides of the bar structure where excess slurry piled up. This resulted in the formation of pores and flaws that would affect the properties of SiC-Sialon refractory. Hence, optimizing printing parameters can effectively reduce these flaws, which will improve the SiC-Sialon refractory properties. Based on the above results, when the nozzle size, air pressure and layer height were selected to be 1.0 mm, 5.8 kPa and 0.5 mm, respectively, green bodies of SiC-Sialon refractory crucible and filter with excellent structures were obtained (Fig. 13).

### 3.3. Microstructure and phase compositions of SiC-Sialon refractory

The phase compositions of SiC-Sialon refractory sintered at different temperatures are shown in Fig. 14. It was observed that the primary phase present in the specimens was SiC. At a temperature of 1400 °C, β-Sialon phase was generated within the matrix. The intensity of diffraction peaks of β-Sialon increased with an increase in the sintering temperature. However, the intensity of corundum diffraction peaks decreased gradually. When the temperature reached 1600 °C, the diffraction peaks of corundum disappeared, because $Al_2O_3$ reacted with

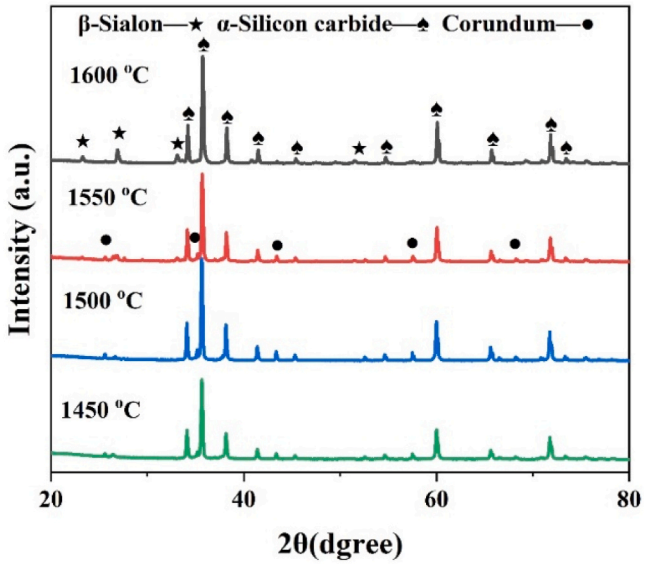


**Fig. 14.** XRD indicating the phase compositions of the SiC-Sialon refractory sintered at different temperatures.

$SiO_2$ and $N_2$ to generate Sialon at high temperatures.

The fracture surfaces of the SiC-Sialon refractory sintered at different temperatures were examined and SEM images of them are presented in Fig. 15. At a temperature of 1300 °C, there were numerous pores within the matrix due to the poor sintering of SiC particles. As the temperature increased, the specimens became denser gradually because higher temperatures facilitated the sintering. Additionally, $Al_2O_3$ reacted with $SiO_2$ and $N_2$ to form Sialon whiskers within the matrix at high temperatures. The growth of Sialon whiskers increased with an increase in temperature. Consequently, the generated Sialon filled the pores in the matrix, which resulted in an improvement in the density of the specimens.

### 3.4. The properties and thermal shock resistance of SiC-Sialon refractory

Based on the results above, the optimal sintering temperature was 1600 °C. Therefore, the green bodies that were printed and then sintered at this temperature were evaluated for their physical properties. Table 4 shows the physical properties of the SiC-Sialon refractory sintered at 1600 °C. The flexural strength and density of the SiC-Sialon refractory were maintained at high levels. In the SiC-Sialon system, the Sialon phases generated are considered as binder phases that improve the strength of the composite. The dense matrix and generated whiskers significantly improved the mechanical strength of the specimens.

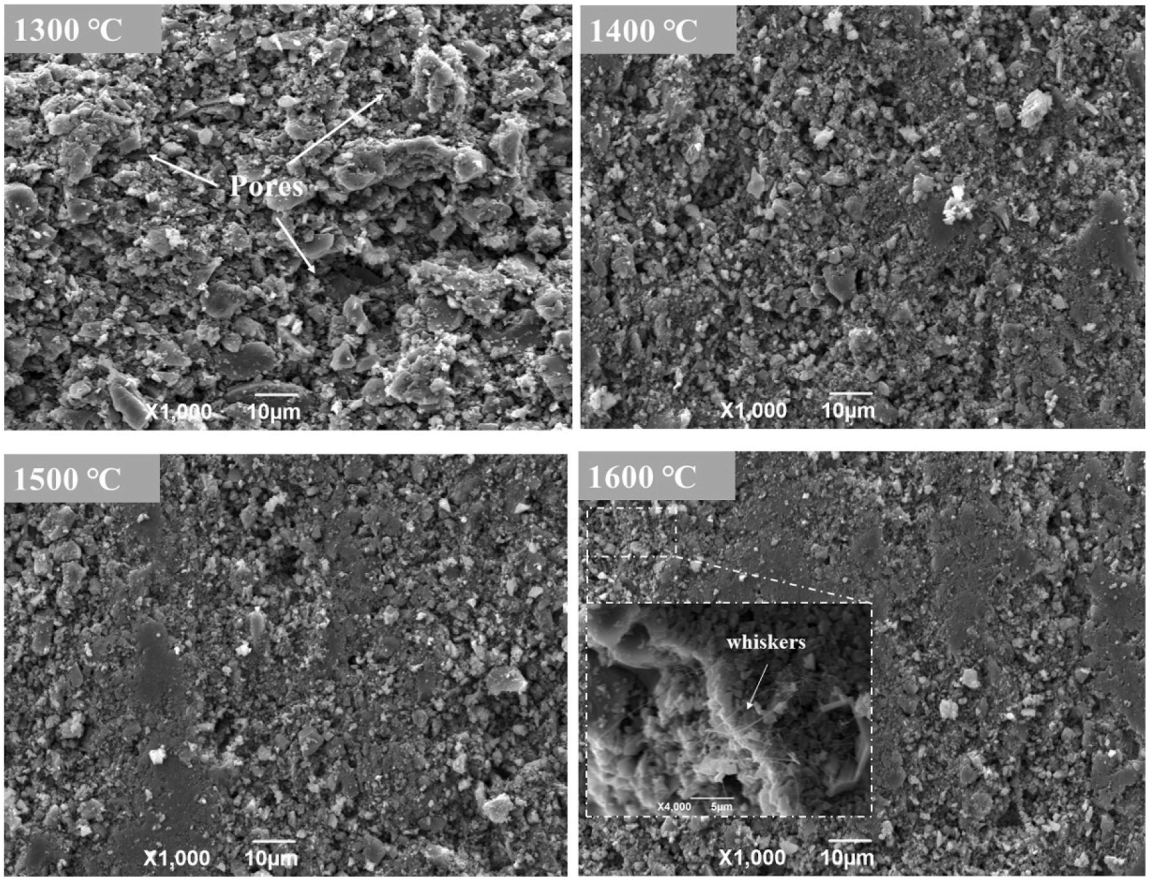


**Fig. 15.** SEM images showing the microstructure of the SiC-Sialon refractory sintered at different temperatures.

**Table 4**
Physical properties of SiC-Sialon refractory sintered at 1600 °C.

| | Apparent Porosity/% | Bulk density/g·cm$^{-3}$ | Flexural strength/MPa | Residual flexural strength/MPa | Residual strength rate/% |
|---|---|---|---|---|---|
| SiC-Sialon refractories | 13.7 | 2.43 | 85 | 57 | 66.7 |

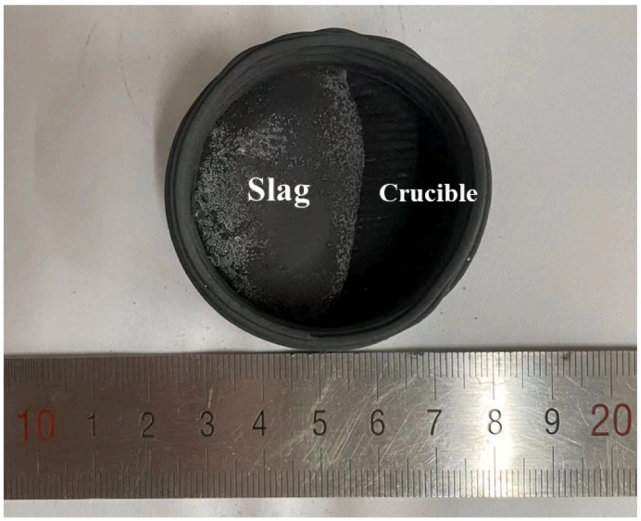


**Fig. 16.** An optical image of the crucible after slag corrosion.

Additionally, the SiC-Sialon refractory manufactured in this work had lower porosity (≤ 13.7%) and better flexural strength (~85 MPa) compared to those fabricated by traditional methods [26–28]. Furthermore, after undergoing thermal shock testing (10 cycles), the residual strength rate of SiC-Sialon refractory was still higher than 66.7%, indicating that the printed SiC-Sialon refractory had excellent thermal shock resistance.

### 3.5. The slag corrosion resistance of SiC-Sialon refractory

The impact of molten iron slag on the corrosion behavior of the printed SiC-Sialon crucible is displayed in Fig. 16. Even after high temperature~1500 °C molten iron slag corrosion, the structure of the crucible remained intact. The microstructure of the corrosion interface between the slag and SiC-Sialon refractory was analyzed, and it was discovered that the molten slag corroded the side wall and bottom of the printed crucible differently (Fig. 17). Energy dispersive X-ray spectroscopy (EDS) analysis revealed that Ca, Mg, and S were homogeneously distributed at the crucible bottom. However, most Ca, Mg, and S were present in the vicinity of the interface between the slag and side wall. As compared to the side wall, a loose area was formed at the bottom of the crucible (Fig. 18). New phases with a whisker structure rich in Mg, Ca,

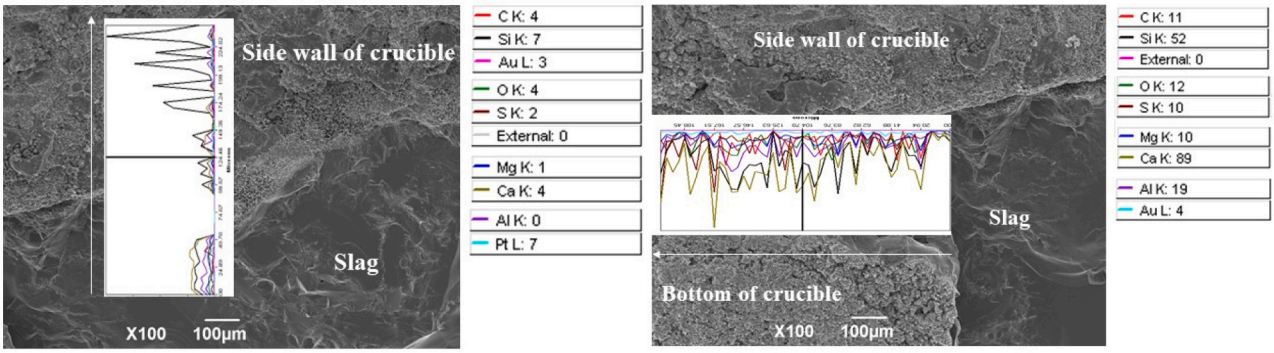


**Fig. 17.** SEM images showing the microstructure of the printed crucible after iron slag corrosion (left: side wall) (right: bottom of crucible), where EDS spectra are presented in the insets.

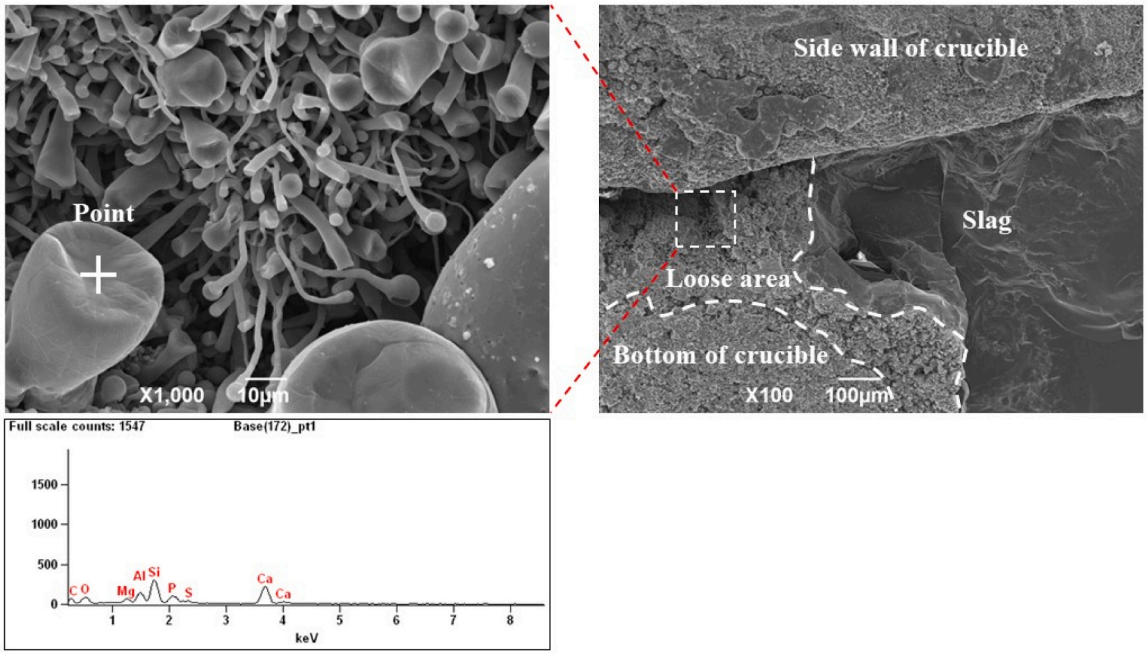


**Fig. 18.** SEM images showing the microstructure of the bottom of the crucible after iron slag corrosion, where an EDS spectrum is also presented.

Al, and Si were found in the corrosion layer at the bottom of the printed crucible, indicating that the molten slag had little corrosion effect on the side wall in comparison with the bottom. Due to the poor wettability between SiC-Sialon and molten slag, the slag was prevented from adhering to the side wall of the crucible, thereby hindering any reaction between them. However, under the action of gravity, the molten slag with low viscosity was more likely to fill into the pores at the crucible bottom and react with the SiC-Sialon to form new phases. The slag corrosion caused a volume expansion of the SiC-Sialon, leading to gaps between the generated whiskers, which further accelerated the corrosion of the crucible bottom by slag.

## 4. Conclusions

SiC-Sialon refractory with complex geometries were additively manufactured using the direct ink writing technique. The rheology and thixotropy of the slurries were optimized by adjusting the particle size of SiC powders, solids content, and additive contents (dispersant and binder). The ideal solid composition for printing was found to be 57 wt% 3.5 μm SiC, 22.13 wt% 0.65 μm SiC, 14 wt% $Al_2O_3$, and 6 wt% $SiO_2$. Additionally, the optimal amounts of dispersant and binder were found to be 0.1 wt% and 2.8 wt%, respectively. The relationships between printing parameters and the geometry of SiC-Sialon refractory were established. When nozzle size, air pressure, and layer height were set to 1.0 mm, 5.8 kPa, and 0.5 mm, respectively, SiC-Sialon refractory with complex geometries and high precision were successfully manufactured. The density, flexural strength, and residual flexural strength rate of the SiC-Sialon refractory sintered at 1600 °C were 2.43 g·cm$^{-3}$, 85.3 MPa, and 66.7%, respectively. The manufactured SiC-Sialon refractory also exhibited excellent resistance to molten iron slag corrosion. The molten slag had little effect on the side wall of the printed SiC-Sialon crucible in comparison with the crucible bottom. Therefore, compared with traditional techniques for manufacturing SiC-Sialon refractory, direct ink writing is an ideal technique for producing SiC-Sialon refractory with complex geometries and excellent properties.

## Declaration of competing interest

We declare that we have no known competing financial interests or personal relationships that could have appeared to influence the work reported in this paper.

## Acknowledgements

This work was supported by the Open Foundation of the State Key Laboratory of Refractories and Metallurgy (No. G202204), Natural Science Foundation of Anhui Provincial Education Department (KJ2020A0270). Open Foundation of the State Key Laboratory of Advanced Refractories (SKLAR202102).

## References

[1] G. Routschka, Refractory Materials: Pocket Manual; Design, Properties, Testing, Vulkan-Verlag GmbH, 2008.
[2] T.P. Nguyen, M.G. Kakroudi, M.S. Asl, Z. Ahmadi, A.S. Namini, S.A. Delbari, Q. V. Le, M. Shokouhimehr, Influence of SiAlON addition on the microstructure development of hot-pressed ZrB2–SiC composites. Ceram. Int. 46 (2020) 19209–19216.
[3] J.A. Lewis, J.E. Smay, J. Stuecker, J. Cesarano, Direct ink writing of three-dimensional ceramic structures. J. Am. Ceram. Soc. 89 (2006) 3599–3609.
[4] C. Jiao, J. Gu, Y. Cao, D. Xie, H. Liang, R. Chen, T. Shi, L., C. Wang, Z. Tian, X. Yi, Preparation of $Al_2O_3$-$ZrO_2$ scaffolds with controllable multi-level pores via digital light processing, J. Eur. Ceram. Soc. 40 (2020) 6087–6094.
[5] J.A. Gonzalez, J. Mireles, Y. Lin, R.B. Wicker, Characterization of ceramic components fabricated using binder jetting additive manufacturing technology, Ceram. Int. 42 (2016) 10559–10564.
[6] P. Bertrand, F. Bayle, C. Combe, P. Gœuriot, I. Smurov, Ceramic components manufacturing by selective laser sintering, Appl. Surf. Sci. 254 (2007) 989–992.
[7] K. Zhu, D. Yang, Z. Yu, Y. Ma, S. Zhang, R. Liu, J. Li, J. Cui, H. Yuan, Additive manufacturing of $SiO_2$–$Al_2O_3$ refractory products via direct ink writing. Ceram. Int. 46 (2020) 27254–27261.
[8] Z. Yu, D. Yang, H. Yuan, Y. Cui, G. Shao, L. Yuan, J. Hu, S. Shang, Effect of $Y_2O_3$ powder on properties of corundum refractory printed by layered extrusion printing, J. Chin. Ceram. Soc. 48 (2020) 1982–1987.
[9] Y. Zhang, Y. Zhang, W. She, L. Yang, G. Liu, Y. Yang, Rheological and harden properties of the high-thixotropy 3D printing concrete, Constr. Build. Mater. 201 (2019) 278–285.
[10] A.M. Guzmán, D.I. Martínez, R. González, Corrosion–erosion wear of refractory bricks in glass furnaces. Eng. Fail. Anal. 46 (2014) 188–195.
[11] A. Bratten, R. Chen, J. Rittenhouse, M. Leu, H. Wen, Improved additive manufacturing of silicon carbide parts via pressureless electric field-assisted sintering, Int. J. Appl. Ceram. Tec. 19 (2022) 2480–2488.
[12] C.C. Furnas, Grading aggregates-I.-Mathematical relations for beds of broken solids of maximum density, Ind. Eng. Chem. 23 (1931) 1052–1058.
[13] W. Jia, Y. Wang, D. Hei, R. Chen, S. Li, Effect of the amount of andalusite addition on the properties of lightweight porous reticulated materials, Constr. Build. Mater. 213 (2019) 257–264.
[14] H. Xing, B. Zou, X. Liu, X. Wang, Q. Chen, X. Fu, Y. Li, Effect of particle size distribution on the preparation of ZTA ceramic paste applying for stereolithography 3D printing, Powder Technol. 359 (2020) 314–322.
[15] P. Kumar, P.C. Kapur, D.N. Saraf, Effect of zeta potential on apparent viscosity of settling suspensions, Colloid Polym. Sci. 253 (1975) 738–743.
[16] L. Guo, J. Yang, Y. Feng, T. Qiu, B. Chen, W. Wan, Preparation and properties of AlN ceramic suspension for non-aqueous gel casting, Ceram. Int. 42 (2016) 8066–8071.
[17] R. Chen, A. Bratten, J. Rittenhouse, T. Huang, W. Jia, M.C. Leu, H. Wen, Additive manufacturing of complexly shaped SiC with high density via extrusion-based technique–effects of slurry thixotropic behavior and 3D printing parameters. Ceram. Int. 48 (2022) 28444–28454.
[18] N. Özkan, C. Oysu, B.J. Briscoe, I. Aydin, Rheological analysis of ceramic pastes, J. Eur. Ceram. Soc. 19 (1999) 2883–2891.
[19] H. Elsayed, A. Chmielarz, M. Potoczek, T. Fey, P. Colombo, Direct ink writing of three dimensional Ti2AlC porous structures, Addit. Manuf. 28 (2019) 365–372.
[20] R. Chen, W. Jia, D. Hei, Y. Wang, Toward excellent performance of $Al_2O_3$-$ZrO_2$ reticulated porous ceramics: new insights based on residual stress, Ceram. Int. 44 (2018) 21478–21485.
[21] J. Yang, J. Lian, Q. Dong, Q. Guan, J. Chen, Z. Guo, Synthesis of YSZ nanocrystalline particles via the nitrate–citrate combustion route using diester phosphate (PE) as dispersant, Mater. Lett. 57 (2003) 2792–2797.
[22] D. Lao, W. Jia, S. Li, D. Hei, R. Chen, Effect of residual compressive stress on thermal shock resistance and microstructure of $Al_2O_3$–$ZrO_2$ reticulated porous ceramics. Mater. Res. Express 6 (2019), 105209.
[23] C.L. Berli, D. Quemada, A. Parker, Modelling the viscosity of depletion flocculated emulsions, Colloid Surf. A. 203 (2002) 11–20.
[24] A. Benchabane, K. Bekkour, Rheological properties of carboxymethyl cellulose (CMC) solutions, Colloid Polym. Sci. 286 (2008) 1173–1180.
[25] F.B. Holness, A.D. Price, Direct ink writing of 3D conductive polyaniline structures and rheological modelling, Smart. Mater. Struct. 27 (2017), 015006.
[26] J. She, T. Ohji, Z.Y. Deng, Thermal shock behavior of porous silicon carbide ceramics, J. Am. Ceram. Soc. 85 (2002) 2125–2127.
[27] S. Ding, Y.P. Zeng, D. Jiang, Thermal shock resistance of in situ reaction bonded porous silicon carbide ceramics, Mater. Sci. Eng. A-Struct. 425 (2006) 326–329.
[28] J.H. She, Z.Y. Deng, J. Daniel-Doni, T. Ohji, Oxidation bonding of porous silicon carbide ceramics, J. Mater. Sci. 37 (2002) 3615–3622.